RESEARCH ARTICLE
SOLID EARTH: GEODYNAMICS

Earth and Planetary Physics
7: 269–281, 2023
doi: 10.26464/epp2023032

Aseismic ridge subduction and flat subduction: Insights from three-dimensional numerical models

Hui Zhao[1,2], and Wei Leng[1,2*]

[1]Laboratory of Seismology and Physics of Earth's Interior, School of Earth and Space Sciences, University of Science and Technology of China, Hefei 230026, China;

[2]Chinese Academy of Sciences Center for Excellence in Comparative Planetology, Hefei 230026, China

Key Points:

- An aseismic ridge needs to be wide and thick enough to induce notable flat subduction.
- Parallel aseismic ridge subduction or double aseismic ridge subduction has a similar effect as super-wide aseismic ridge subduction.
- The flat subduction observed in Chile and Peru can be explained by parallel and double aseismic ridge subduction.

Citation: Zhao, H., and Leng, W. (2023). Aseismic ridge subduction and flat subduction: Insights from three-dimensional numerical models. *Earth Planet. Phys.*, *7*(2), 269–281. http://doi.org/10.26464/epp2023032

Abstract: Flat subduction can significantly influence the distribution of volcanism, stress state, and surface topography of the overriding plate. However, the mechanisms for inducing flat subduction remain controversial. Previous two-dimensional (2-D) numerical models and laboratory analogue models suggested that a buoyant impactor (aseismic ridge, oceanic plateau, or the like) may induce flat subduction. However, three-dimensional (3-D) systematic studies on the relationship between flat subduction and buoyant blocks are still lacking. Here, we use a 3-D numerical model to investigate the influence of the aseismic ridge, especially its width (which is difficult to consider in 2-D numerical models), on the formation of flat subduction. Our model results suggest that the aseismic ridge needs to be wide and thick enough to induce flat subduction, a condition that is difficult to satisfy on the Earth. We also find that the subduction of an aseismic ridge parallel to the trench or a double aseismic ridge normal to the trench has a similar effect on super-wide aseismic ridge subduction in terms of causing flat subduction, which can explain the flat subduction observed beneath regions such as Chile and Peru.

Keywords: flat subduction; aseismic ridge; oceanic plateau; 3-D numerical simulation

1. Introduction

The slab dip angle is one of the most important characteristics of a subduction zone. The dip angle of a subducting slab strongly influences the overriding plate strain and stress state (Lallemand et al., 2005; Chen YW et al., 2019), which in turn affects the surface topography, tectonic regimes (Horton, 2018), and occurrence of earthquake aftershocks and large tsunamis (Oryan and Buck, 2020). The subducting slab dip angle varies among subduction zones worldwide and can even be different along a single subduction zone (Lallemand et al., 2005; Skinner and Clayton, 2011; Hu JS et al., 2018). Typically, when the subducting slab underthrusts closely beneath the overriding plate for a certain distance, a flat subduction zone is developed (Yan ZY et al., 2020). Such flat subduction zones usually lead to (1) a gap in the overriding plate volcanism because of the closeness of the mantle wedge between the subducting slab and the overriding plate (Kay and Mpodozis, 2002; Ramos et al., 2002); (2) intense shortening of the overriding plate above the flat slab segment (Horton, 2018; Chen YW et al., 2019); and (3) high topography at the front edge of the overriding plate (Hampel et al., 2004; Horton, 2018).

Two typical examples of flat subduction zones are those located in Peru and central Chile (Gutscher et al., 2000; Antonijevic et al., 2015; Manea et al., 2017; Jang et al., 2019; Linkimer et al., 2020; Figure 1a). Seismic tomography results show that the Nazca Plate thrusts closely beneath the overriding South American Plate in Peru, leaving a flat slab segment that is more than 1,000 km wide and ~300 km in length at ~120 km depth (Gutscher et al., 1999; Antonijevic et al., 2015; Manea et al., 2017; Jang et al., 2019). Seismic tomography studies also indicate a flat slab segment beneath central Chile that is ~200 km wide and ~300 km in length (Manea et al., 2017; Gutscher et al., 2000; Linkimer et al., 2020). The high topography of the Andes Mountains along the western margin of the South American Plate (Tozer et al., 2019) and the gap in volcanism distribution (Global Volcanism Program) are major characteristics of flat subduction (Figure 1a). Some other flat subduction zones are also found worldwide. Gutscher (2001) proposed that an ~400-km-long flat slab segment exists beneath the Nankai Trough (southwest Japan) (Figure 1b). Manea et al. (2017) suggested that an ~150-km-long flat slab segment lies beneath Mexico. On the basis of tomography results, Liu LJ et al. (2010) calculated an inverse mantle convection model and suggested that the Farallon Plate subducted horizontally beneath

Correspondence to: W. Leng, wleng@ustc.edu.cn
Received 30 DEC 2022; Accepted 20 FEB 2023.
Accepted article online 08 MAR 2023.

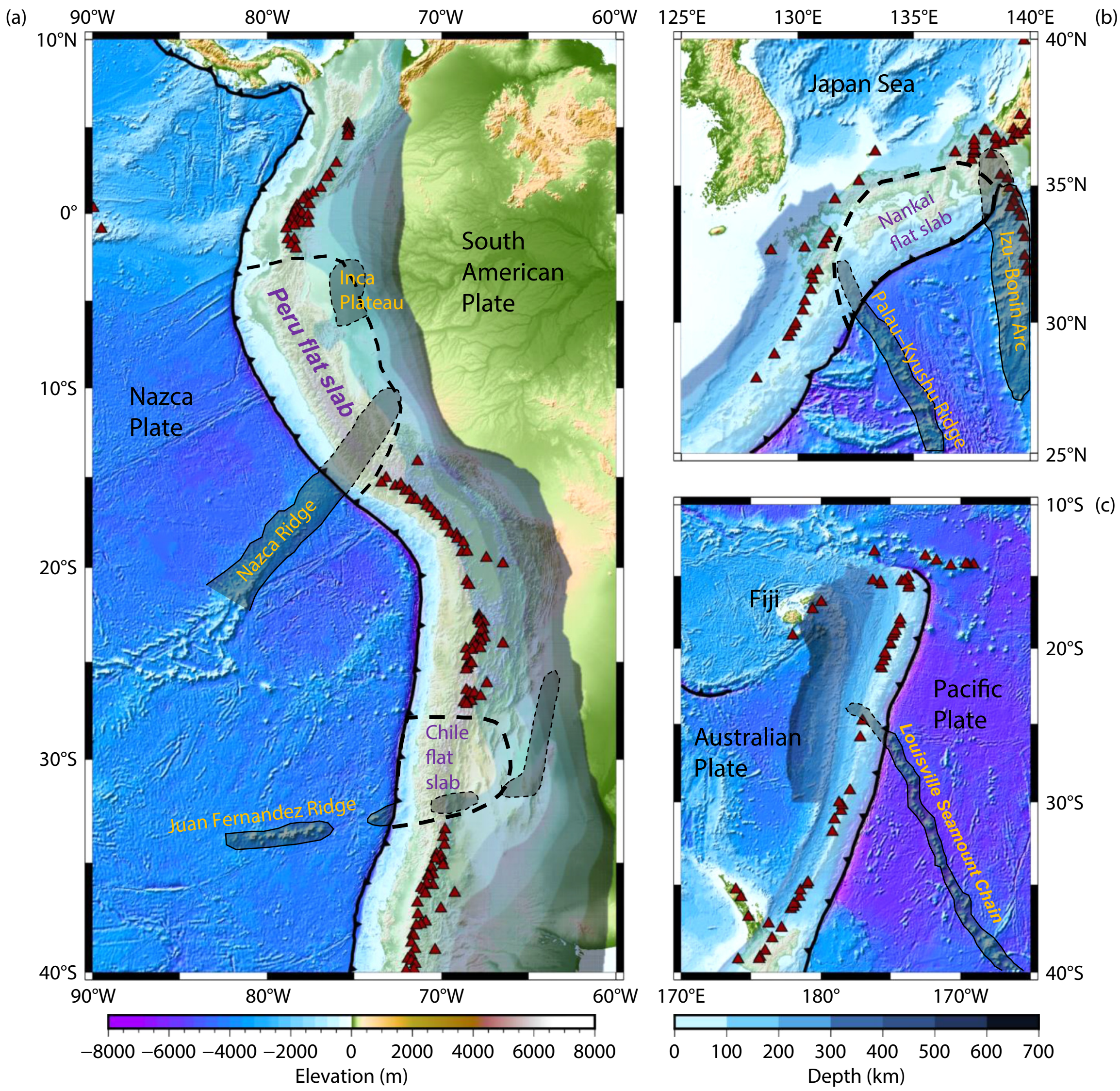

Figure 1. Regional map of (a) Peru and Chile flat subduction, (b) Nankai flat subduction, and (c) Tonga–Kermadec subduction. The background color represents topography and bathymetry (Tozer et al., 2019). The shaded depth contours show the geometry of the subducting slab (Hayes et al., 2018). The flat slab areas are outlined by thick dashed lines and labeled with purple characters. Red triangles show the distribution of volcanic eruptions. The buoyant impactors (e.g., aseismic ridge, seamount chain) are represented with shadow areas and yellow characters that are circled by thin solid or dashed lines above or beneath the Earth's surface.

the North American Plate and formed a flat subduction zone at ~70 Myr ago. Furthermore, Li ZX and Li XH (2007) and Yan ZY et al. (2020) suggested that flat subduction occurred beneath South China between 250 and 190 Myr ago, to explain the origin of the South China Orogenic Belt.

Various mechanisms have been proposed to explain the formation of flat subduction zones, including the subduction of buoyant impactors (e.g., aseismic ridges, seamount chains, and oceanic plateaus; Gutscher et al., 1999; Gerya et al., 2009), the structure of the overriding plate (Taramón et al., 2015; Liu SB and Currie, 2016), the absolute motion of the plates (van Hunen et al., 2002; Espurt et al., 2008), the delay in the basalt to eclogite transition caused by the cold thermal structure of the overlapping lithospheres (Gutscher et al., 2000), the existence of a sub-slab buoyant asthenosphere (Hawley et al., 2016; Portner et al., 2017; Bodmer et al., 2018; Fan JK and Zhao DP, 2021), and interplate hydrostatic suction (Jischke, 1975). Among these mechanisms, the subduction of buoyant impactors is an inescapable factor because of the obvious correlation between the distribution of buoyant impactors and flat subduction zones (Lallemand et al., 2005; Antonijevic et al., 2015). The Peru flat subduction correlates to the subducting Nazca Ridge, and the "lost Inca Plateau," which has been entirely subducted into the asthenospheric mantle (Gutscher et al., 1999; Bishop et al., 2017; Figure 1a); the central Chile flat subduction correlates to the subducting Juan Fernández Ridge (Yáñez et al., 2001; Espurt et al., 2008; Figure 1a); the Nankai flat subduction zone correlates to the Palau–Kyushu Ridge and Izu–Bonin Arc (Gutscher, 2001; Figure 1b); and the Farallon flat slab segment correlates to the Shatsky and Hess oceanic plateaus carried by the old Farallon Plate at ~90–70 Myr ago (Liu LJ et al., 2010; Liu SB and Currie, 2016). However, in the Tonga–Kermadec subduction zone, no flat slab has been detected at the location where the Louisville

Seamount Chain intersects with the trench (Bonnardot et al., 2007; Figure 1c). Thus, the influence of a buoyant impactor on flat subduction needs to be investigated further.

Many two-dimensional (2-D) numerical models (van Hunen et al., 2002; Gerya et al., 2009; Tetreault and Buiter, 2012; Vogt and Gerya, 2014; Huangfu PP et al., 2016; Yan ZY et al., 2021, 2022) have been used to investigate the influence of an aseismic ridge (or an oceanic plateau) on the occurrence of flat subduction. However, it is difficult to consider the width of an aseismic ridge in a 2-D numerical model because of its intrinsic geometric limit, namely that the aseismic ridge is assumed to be infinitely wide in a 2-D model. On the other hand, the width of aseismic ridges has been suggested to be one of the key factors controlling the slab dip angle in laboratory analogue models (Martinod et al., 2013; Flórez-Rodríguez et al., 2019). Therefore, the previous 2-D numerical models may overestimate the effects of aseismic ridge subduction with a finite width. Several three-dimensional (3-D) numerical models have been proposed to explore the mechanisms of flat subduction. Taramón et al. (2015) suggested that the thickness of the overriding plate can influence the formation and evolution of flat slabs. Rodríguez-González et al. (2014) suggested that the thermal structure of the overriding plate can also modify the dip angle of the subducting slab. Besides the structure of the overriding plate, the aseismic ridge or oceanic plateau has been suggested as one of the key factors influencing the slab dip angle (Martinod et al., 2013; Flórez-Rodríguez et al., 2019), and some 3-D numerical models have been proposed to study the interaction of an oceanic plateau and the subduction zone. Mason et al. (2010) investigated the influence of the density and rheology of the oceanic plateau on the evolution of trench geometry and the occurrence of a slab window. Moresi et al. (2014) explored the influence of a ribbon-like microcontinent on trench geometry. Betts et al. (2015) used 3-D numerical models to study the combined influence of the oceanic plateau and the plume head on trench geometry and slab tear. However, the influence of a buoyant impactor on the slab dip angle was not the key focus of their study. Furthermore, several researchers using 3-D numerical models have suggested that the oceanic plateau or aseismic ridge can induce flat subduction; however, these studies have examined only specific regions and have not investigated the influence of different properties of the buoyant impactor on the subduction process (Liu LJ et al., 2010; Hu JS et al., 2016). Thus, the relationship between the width of a buoyant impactor and flat subduction needs further systematic study with 3-D numerical models.

Here, we used a 3-D numerical model to systematically investigate the influence of an aseismic ridge, especially its width, on flat subduction. We suggest that the aseismic ridge must be more than 400 km in width to support a large flat slab segment. However, such a super-wide aseismic ridge is rarely observed on the Earth's surface. We thus propose two alternative ways to induce flat subduction with narrow aseismic ridges, trench-parallel ridge subduction or double aseismic ridge subduction, which can explain the geological and seismic observations in the central Chile, Peru, and Nankai flat subduction zones.

2. Method

We developed a 3-D numerical model to investigate the influence of an aseismic ridge with a finite width on the subducting slab geometry. We used a modified finite element code, CitcomCU (adding the particle tracing method, considering elasticity, etc.), to solve the conservation equations of mass, momentum, and energy (Zhong SJ, 2006; Leng W and Gurnis, 2015). For the detailed methodology, see Leng W and Gurnis (2011) and Leng W and Gurnis (2015).

The size of our model was $2{,}640 \times 1{,}320 \times 660$ km (*X*, *Y*, and *Z* directions; Figure 2). Using the "particle in cell" method, we could effectively calculate a 3-D numerical model with a relatively low resolution. We divided our model into $512 \times 64 \times 128$ grids (leading to a model resolution of $5.16 \times 20.63 \times 5.16$ km) in the *X*, *Y*, and *Z* directions, and we set 27 particles in each element. We verified the reliability of our model results by performing a resolution test (Figure S1). That is, we increased the model resolution to $2.58 \times 10.31 \times 2.58$ km in the *X*, *Y*, and *Z* directions and found that the model results were almost identical to those from the reference model (Figure S1b, c). However, when we decreased the model resolution to $10.31 \times 41.25 \times 10.31$ km in the *X*, *Y*, and *Z* directions, a large discrepancy was found compared with the reference model (Figures S1a, b).

In our model, the half-widths of the subducting plate and the overriding plate were both 1,254 km (representing a 2,508-km-wide plate owing to reflective boundary conditions), and the lengths of the subducting plate and the overriding plate were 1,306 km and 1,202 km, respectively (Figure 2a). The plates were detached from the boundary walls by weak zones between the plate margins and model boundaries. The thickness of the overriding continental plate was 100 km, with a 20-km-thick upper continental crust and a 20-km-thick lower continental crust (Figure 2b). The thickness of the subducting oceanic plate was controlled by the age of the oceanic plate (Glerum et al., 2018), and the thickness of the oceanic crust was 8 km. We set the aseismic ridge on the subducting plate by considering a regional thickened oceanic crust, and the geometry of the aseismic ridge varied among different cases (Figures 2a, b).

For the surface and the bottom, we used isothermal boundary conditions and ignored the adiabatic heating gradient. The surface temperature was 0 °C, and the bottom temperature was 1,400 °C. We used a half-space cooling model to calculate the initial temperature field of the subducting oceanic plate, and we set a linear temperature field for the overriding continental plate. According to results of the reconstructed oceanic plate age (Capitanio et al., 2011; Hu JS et al., 2016; Müller et al., 2016), we used 40 Myr as the initial age of the subducting plate in our reference model, simulating the subduction beneath Peru and Chile. We prescribed a far-field velocity field at the cross section of the subducting slab, 800 km away from the left boundary wall, to induce subduction (Figure 2c). Reflective boundary conditions were applied to all lateral boundaries of the model, in which the waves reflected off the boundaries. By using reflective boundary conditions, we needed to calculate only half the model domain because the simulations were geometrically symmetrical with respect to the reflective boundary wall. In addition, free-slip boundary conditions were applied to the top and bottom boundaries.

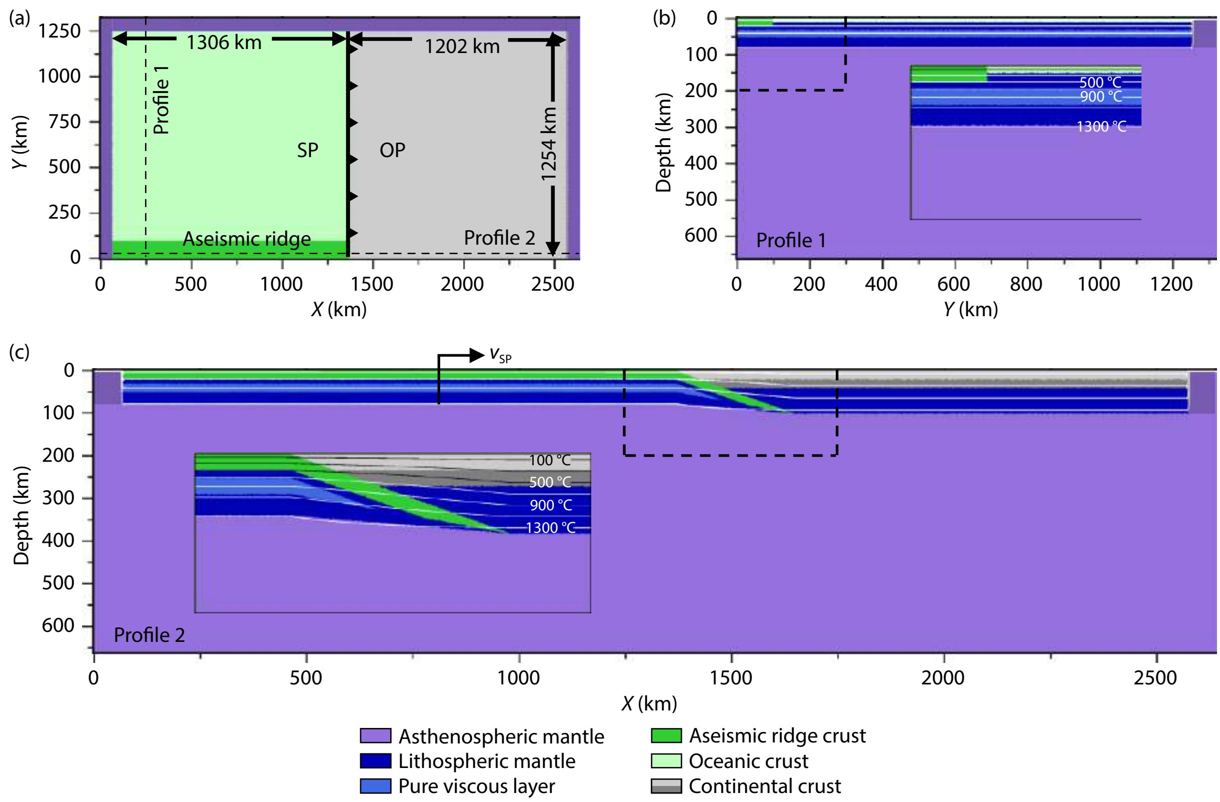

Figure 2. Model setup. (a) Top view of our model, including a subducting plate (SP; light green area) and an overriding plate (OP; light gray area), both of which are detached from the boundary walls by weak zones (dark purple area). Profile 1 is a cross section perpendicular to the X axis, and Profile 2 is a cross section perpendicular to the Y axis. (b) Composition and temperature field along Profile 1, representing the structure of the subducting plate. The subplot shows the thicker oceanic crust of the aseismic ridge (dark green area) and the thinner oceanic crust elsewhere (light green area). The contours show the temperature structure of the subducting plate calculated from the half-space cooling model. (c) Composition and temperature field along Profile 2. The subplot shows the transition between the subducting plate and the overriding plate. The color codes of the different materials can be found in the key below.

The rheological properties in our model were similar to those of Leng W and Gurnis (2015) and Zhao H et al. (2021). The non-Newtonian viscosity was calculated by using Equation (1), which is both temperature and stress dependent:

$$\eta = \eta_0 \left(\frac{\dot{\varepsilon}_{II}}{\dot{\varepsilon}_0}\right)^{\left(\frac{1}{n}-1\right)} \exp\left[\frac{E}{nR}\left(\frac{1}{T}-\frac{1}{T_0}\right)\right], \tag{1}$$

where, η_0, $\dot{\varepsilon}_{II}$, $\dot{\varepsilon}_0$, E, n, R, T, and T_0 represent the reference viscosity, second invariant of the deviatoric strain rate tensor, reference strain rate, activation energy, strain exponent, gas constant, absolute temperature, and reference temperature, respectively. We also constrained the value of viscosity between [η_{min}, η_{max}] for numerical convergency and efficiency. Here, we used the dry olivine flow law, the wet quartzite flow law, and the plagioclase An_{75} flow law to describe the rheology of the mantle, continental crust, and aseismic ridge crust, respectively (Ranalli, 1995). We weakened the surface 8 km of the subducting plate (entire oceanic crust and the uppermost 8 km of the aseismic ridge crust) by setting its viscosity as η_{min} to facilitate the decoupling between the subducting plate and the overriding plate. In addition, we set a purely viscous strong core whose viscosity was η_{max} in the subducting plate to avoid slab break-off during the subduction process (Schellart and Moresi, 2013; Zhao H et al., 2021; light blue area in Figure 2c). The values of the model parameters can be found in Table 1.

For plastic rheology, the yield stress, τ_y, could be expressed by Equation (2):

$$\tau_y = \mu P + C, \tag{2}$$

where μ, C, and P represent the coefficients of friction, cohesion, and pressure, respectively. In our model, the value of the friction coefficient, μ, and cohesion, C, both decreased with accumulated plastic strain (Buck and Poliakov, 1998). We used Equations (3) and (4) to describe such strain-weakening effects:

$$\mu = \mu_0\left[1-\min\left(1, \frac{\varepsilon_p}{\varepsilon_f}\right)\right], \tag{3}$$

$$C = C_f + (C_0 - C_f)\left[1-\min\left(1, \frac{\varepsilon_p}{\varepsilon_f}\right)\right], \tag{4}$$

where μ_0, C_0, C_f, ε_p, and ε_f represent the initial coefficient of friction, initial cohesion, minimum cohesion, accumulated plastic strain, and reference plastic strain, respectively.

3. Results

3.1 Reference Model

In our reference model, the crust of the aseismic ridge was 20 km thick and 200 km wide (the half-width was 100 km in our model).

Table 1. Model constants.

Parameter name	Symbol	Value
Reference mantle density	ρ_0	3,300 kg·m^{-3}
Oceanic crust density	ρ_{oc}	2,900 kg·m^{-3}
Upper continental crust density	ρ_{uc}	2,800 kg·m^{-3}
Lower continental crust density	ρ_{lc}	3,000 kg·m^{-3}
Reference temperature	T_0	1,400
Reference viscosity	η_0	10^{20} Pa·s
Strain exponent (mantle)	n_m	3.5
Strain exponent (continental crust)	n_c	2.3
Strain exponent (aseismic ridge crust)	n_a	3.2
Reference strain rate	$\dot{\varepsilon}_0$	10^{-15} s^{-1}
Gas constant	R	8.31 J·mol^{-1}
Activation energy (mantle)	E_m	540 kJ·mol^{-1}
Activation energy (continental crust)	E_c	154 kJ·mol^{-1}
Activation energy (aseismic ridge crust)	E_a	238 kJ·mol^{-1}
Minimum viscosity	η_{min}	10^{20} Pa·s
Maximum viscosity	η_{max}	10^{24} Pa·s
Initial coefficient of friction	μ_0	0.5
Initial cohesion	C_0	40 MPa
Minimum cohesion	C_f	1 MPa
Reference plastic strain	ε_f	0.3

We prescribed a far-field plate velocity of 5 cm/yr to initiate the subduction process and fix the overriding plate. Figure 3 shows the evolution of the subducting slab geometry along with the dynamic slab dip angle in the reference model. Here, we defined the dynamic dip angle, θ, at each point as

$$\theta = \frac{v_z}{\sqrt{v_x^2 + v_y^2}}, \tag{5}$$

where v_x, v_y, and v_z represent velocities in the X, Y, and Z directions at each point, respectively.

The evolution of the subduction process in the reference model can be divided into three stages. At the beginning, the subducting plate moves toward the overriding plate at a velocity of 5 cm/yr, and the front tip of the subducting plate starts to bend and thrust into the asthenospheric mantle (Figure 3a). The length of the subducting slab in the asthenosphere then increases, and the dynamic dip angle of the subducting slab varies along the Y direction. The dynamic slab dip angle remains small where the aseismic ridge is located, and the dynamic slab dip angle becomes larger elsewhere (Figure 3b). Finally, the difference in the dynamic slab dip angle becomes more significant along the Y direction. The slab subducts horizontally on the back side because of the buoyancy provided by the aseismic ridge, and it subducts with a large slab dip angle on the front side (Figure 3c). Here, we can also notice that the dynamic dip angle remains small and forms a flat slab segment approximately 200 km long, as labeled in Figure 3c. However, the buoyant aseismic ridge cannot support such a flat slab segment for a long time because of the drag force from the surrounding slab with a large slab dip angle. The front tip of the flat slab segment starts to bend downward at 13.80 Myr (Figure 3c).

3.2 Influence of the Aseismic Ridge Width

We then changed the width of the aseismic ridge to investigate its influence on the subducting slab morphology. Figure 4 shows the results at 13.80 Myr when the aseismic ridge widths are 100, 200, 300 km, and infinity, respectively. When the aseismic ridge is 100 km wide, the slab dip angle is large, and only a slight difference in the slab dip angle is observed along the Y direction, suggesting that the buoyant force provided by the narrow aseismic ridge is insufficient to form notable flat subduction (Figure 4a). Then, when we increased the aseismic ridge width, the slab began to subduct horizontally along the aseismic ridge and form a flat slab segment. A larger aseismic ridge width led to a larger flat slab segment area (Figures 4b–d).

Specifically, when the aseismic ridge width reaches infinity, which is similar to the situation in the 2-D numerical models, the entire subducting slab will thrust closely beneath the overriding continental plate and subduct horizontally, forming a large flat slab segment (Figure 4d). We can conclude, based on the results with different aseismic ridge widths, that a wider aseismic ridge provides a more favorable condition for the occurrence of flat subduction. However, the typical width of the aseismic ridge on the Earth's surface is usually not larger than 200 km. Therefore, the results obtained from 2-D numerical models may overestimate the effects of aseismic ridges on flat subduction (Figure 4).

3.3 Influence of the Crustal Thickness

We then investigated the influence of the crustal thickness of the aseismic ridge on flat subduction. Fixing the width of the aseismic ridge to 200 km, as in the reference model, we varied the thickness of the aseismic ridge crust from 15 to 25 km. Figure 5 shows the geometries of the subducting slabs along Profile 2 (Figure 2) with different crustal thicknesses. The subplot in Figure 5c shows the dynamic slab dip angle distributions along the profile.

Figure 5b shows the results of the reference model along Profile 2 in Figure 2. The subducting slab changes its dip angle and forms an ~200-km-long flat slab segment beneath the overriding plate. Beyond the flat slab segment, the tip of the subducting slab bends down and subducts into the asthenospheric mantle. When we reduced the aseismic ridge crustal thickness to 15 km, the slab dip angle changed only slightly beneath the overriding plate and could not form a flat slab segment compared with the case when the aseismic ridge crust was 20 km thick (Figure 5a, b). In contrast, when the aseismic crustal thickness was increased to 25 km, the slab would thrust beneath the overriding plate, forming a long flat slab segment (Figure 5c). From the subplot in Figure 5c, it can be observed that the dynamic dip angle along the subducting slab is the smallest when the aseismic ridge crustal thickness is 25 km and that it becomes larger when the aseismic ridge crustal thickness is decreased to 20 and 15 km.

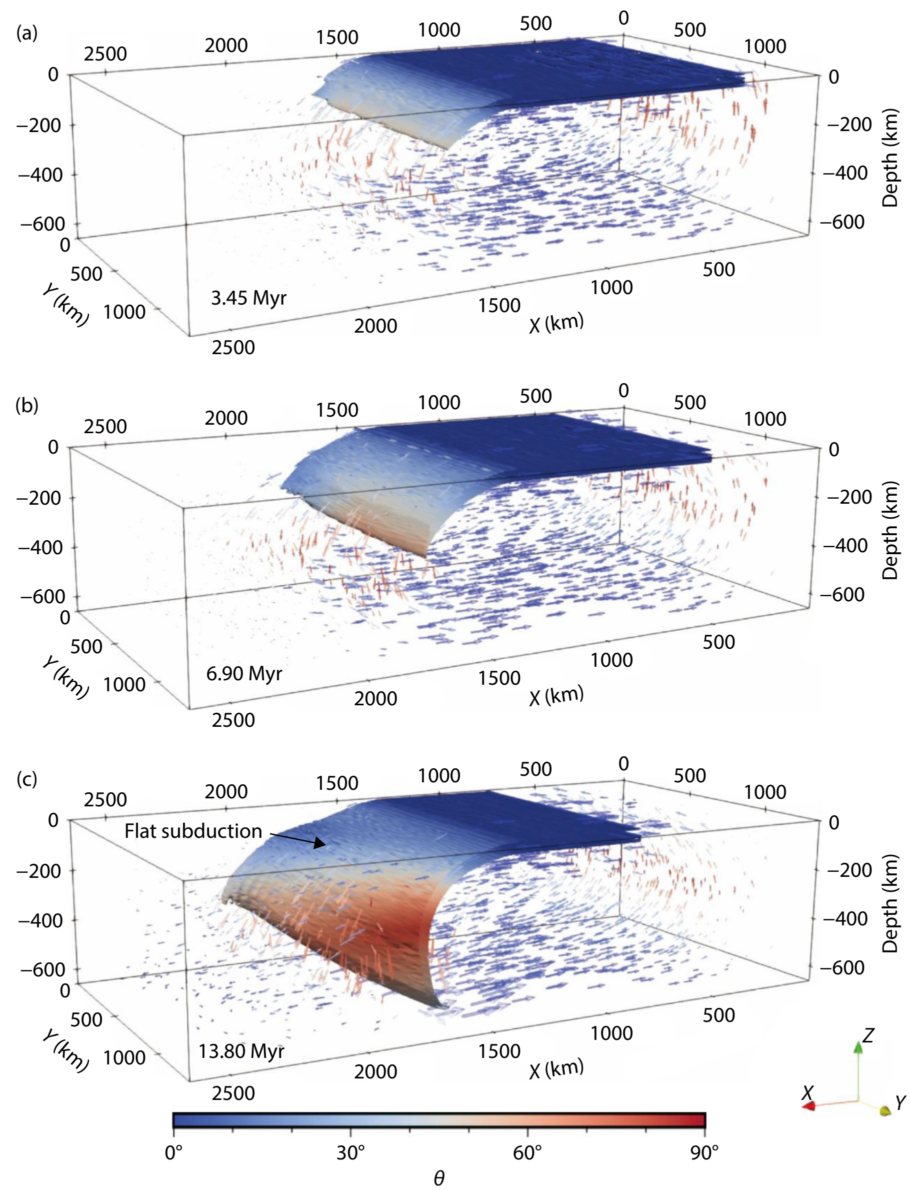

Figure 3. Morphology of the subducting slab at (a) 3.45 Myr, (b) 6.90 Myr, and (c) 13.80 Myr in the reference model. The arrows show the velocity field of the reference model. The colors indicate the dynamic slab dip angle calculated by Equation (5). The blue color indicates that the slab is flat, and the red color indicates that the slab is steep. To show the subducting slab morphology clearly, the asthenosphere and the overriding plate are not displayed here.

As shown from the results above, the formation of the flat slab segment is affected by both the aseismic ridge width and its crustal thickness. We defined the length of the flat slab segment as the movement of the location where the subducting slab and the overriding plate become decoupled in the *X* direction and plotted it versus the aseismic ridge width and its crustal thickness (Figure 6). When the crustal thickness and the aseismic ridge width are small, flat subduction is difficult to form because of the lack of buoyant force (red blocks in Figure 6). In contrast, a thick and wide aseismic ridge can provide favorable conditions for the occurrence of a large, flat slab segment (blue blocks in Figure 6). Therefore, our model results demonstrate that an aseismic ridge needs to be wide and thick enough to induce notable flat subduction.

3.4 Aseismic Ridge Subduction Parallel to the Trench

We also tested the influence of the aseismic ridge orientation on flat subduction because not all aseismic ridges subduct perpendicularly to the trench (Lallemand et al., 2005; Müller et al., 2016). We designed a new model (Figure 7a) in which the aseismic ridge was 100 km long in the *X* direction and its crust was 15 km thick. The impact width of the aseismic ridge was 800 km in the *Y* direction (half-width was 400 km in the model), simulating aseismic ridge subduction parallel to the trench.

Once the aseismic ridge subducts into the mantle, it decreases the slab dip angle because of its buoyant force (Figure 7b). The decrease in slab dip angle inhibits the formation of the mantle wedge, and the coupling between the subducting slab and the overriding plate remains strong. Thus, the slab can continue to

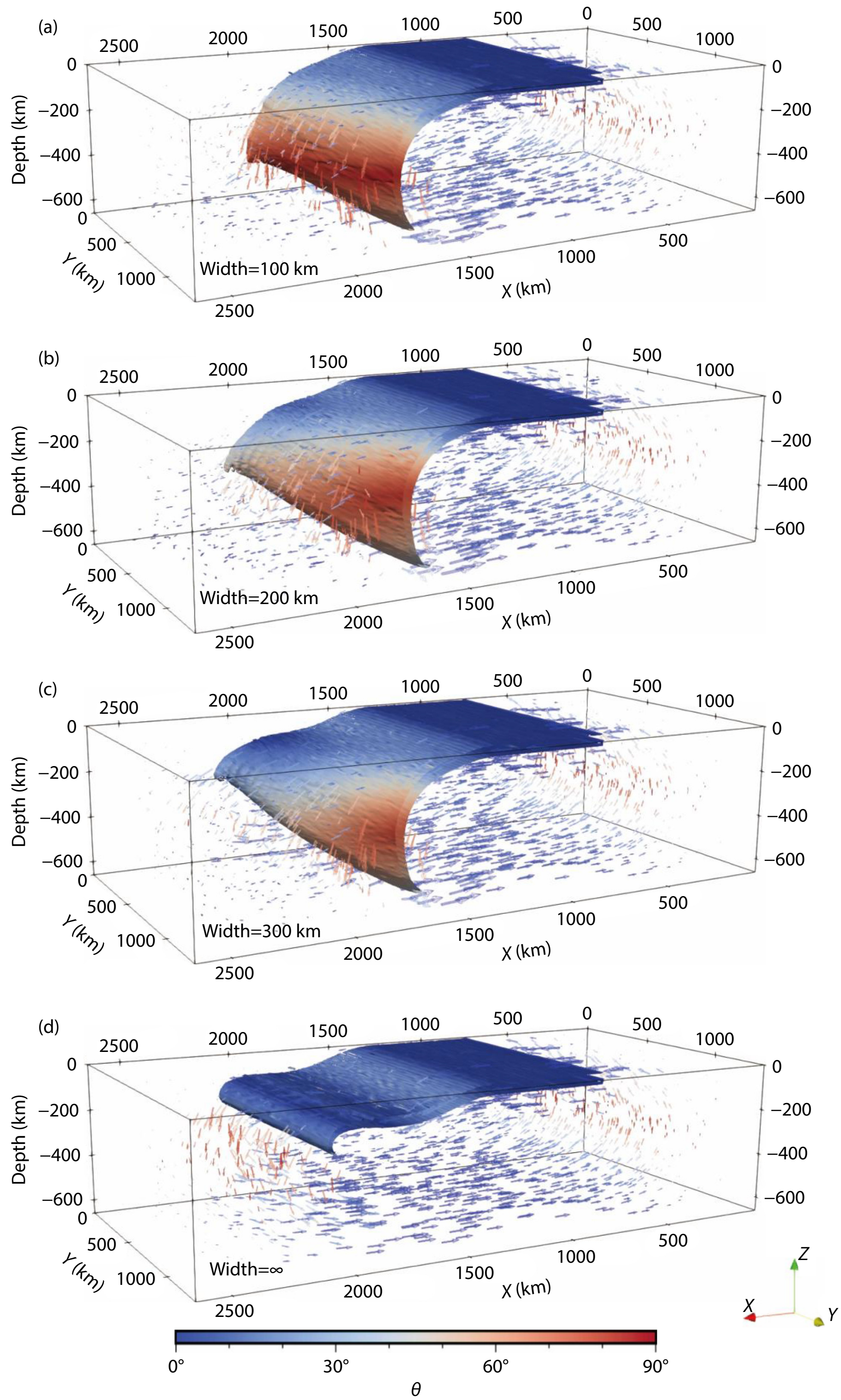

Figure 4. Morphologies of the subducting slabs with aseismic ridges of different widths. The aseismic ridge widths are (a) 100 km, (b) 200 km, (c) 300 km, and (d) infinity. The colors and symbols are the same as those in Figure 3.

subduct horizontally for more than 200 km at 13.80 Myr even though the aseismic ridge is only 100 km long in the *X* direction (Figure 7c). These results show that a narrow aseismic ridge can also cause a notable flat slab segment if it subducts parallel to the trench.

3.5 Subduction of Double Aseismic Ridges

In the previous models, we considered only the effect of a single aseismic ridge. Here, we consider two parallel aseismic ridges to show their effects on flat subduction. Both aseismic ridges are 200 km wide and have a crustal thickness of 20 km, whereas the

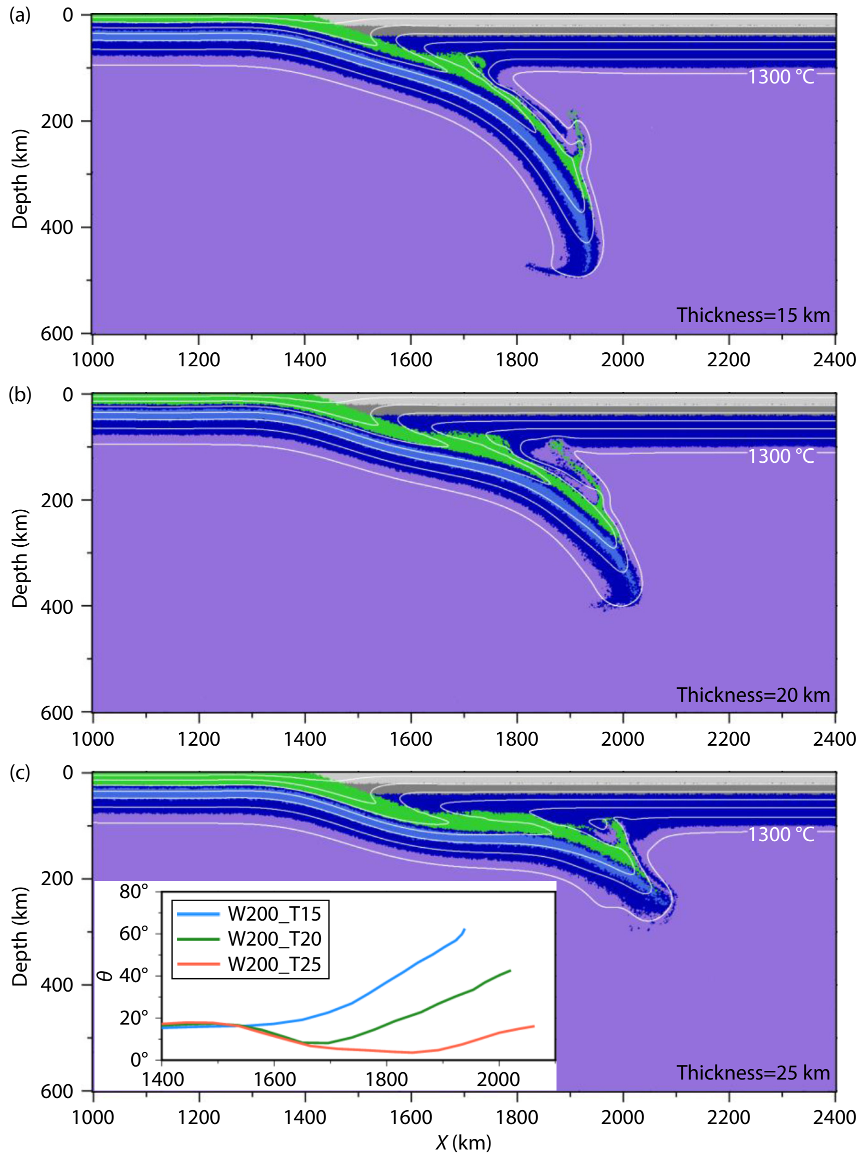

Figure 5. The geometries of the subducting slabs along Profile 2 in Figure 2 with different aseismic ridge crustal thicknesses. The width of the aseismic ridge is fixed at 200 km. The crustal thicknesses of the aseismic ridges are (a) 15 km, (b) 20 km, and (c) 25 km. The white lines are the thermal contours, and the meanings of the different colors can be found in the color code in Figure 2. The subplot shows the dynamic slab dip angle distributions along Profile 2 in Figure 2. The blue, green, and red lines show the results with aseismic ridge crustal thicknesses of 15, 20, and 25 km, respectively.

distance between the two aseismic ridges is 700 km (Figure 8a).

Figure 8b shows the temperature field along the profile after 13.80 Myr of evolution, represented by the dashed line in Figure 8a. Figure 8c represents the slab morphology along with the distribution of the dynamic dip angle. Because of the buoyant force provided by the aseismic ridges, the subducting slab thrusts closely beneath the overriding plate along the aseismic ridges where the slab dip angle reaches its minimum (Figure 8b). The slab dip angle increases gradually toward the edge of the subducting slab, and finally, a flat slab segment more than 900 km wide is formed (Figure 8b, c). Thus, two parallel aseismic ridges can act as one super-wide aseismic ridge and induce a large, flat subduction zone.

We can also observe that the slab dip angle varies in the flat subduction zone. The slab dip angle is the smallest along the two aseismic ridges (Figure 8b, c) and there forms a sag of the subducting slab between the two aseismic ridges because of the lack of buoyant force (Figure 8b). The scale of this sag is strongly affected by the distance between the two aseismic ridges. When the distance between the two aseismic ridges increases, the sag also increases (Figure S2).

4. Discussion

The objective of the numerical models was not to study the geodynamic constraints of a specific region, but rather to gain insights into the probable mechanisms inducing the occurrence of a flat subduction. Nevertheless, we consider our numerical model results to be comparable to several natural flat subduction zones.

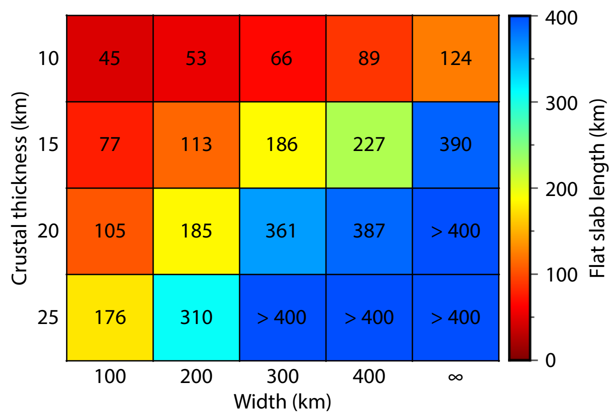

Figure 6. Lengths of the flat slab segments with different aseismic ridge widths and crustal thicknesses. The numbers and corresponding colors represent the lengths of the flat slab segments.

4.1 "Chile-type" Flat Subduction

The results from our model suggest that the buoyant impactor (e.g., aseismic ridge, seamount chain, oceanic plateau) needs to be wide and thick enough to support a significant flat slab segment (Figure 6). However, it is difficult to have such large-scale buoyant impactors on Earth. For example, the Juan Fernández Ridge is generally considered the key factor causing the flat subduction in Chile (Yáñez et al., 2001; Pesicek et al., 2012; Huangfu PP et al., 2016; Figure 1a). However, seismic investigations suggest that the Juan Fernández Ridge is narrow and has a crustal thickness of ~13 km (Kopp et al., 2004). According to our model results (Figure 6), such a thin, narrow ridge would have difficulty supporting the flat subduction in Chile, which is ~200 km wide and ~300 km in length (Manea et al., 2017; Gutscher et al., 2000; Linkimer et al., 2020).

Nevertheless, a significant bend occurred in the Juan Fernández Ridge in its migrating history. Although the Juan Fernández Ridge seems to be subducting perpendicularly to the trench at present, it changed its migrating direction at ~20 Myr ago (Yáñez et al., 2001; Espurt et al., 2008; Bello-González et al., 2018; Linkimer et al., 2020). Such a change in migrating direction caused a large segment of the ridge in the mantle to be subparallel to the trench (Figure 1a), which could have provided a large-width buoyant impactor and probably led to the formation of the flat subduction in Chile (Figure 7). Furthermore, several studies have suggested the existence of a subslab slow-velocity anomaly beneath Chile (Portner et al., 2017; Fan JK and Zhao DP, 2021), which could provide additional buoyancy for the subducting Nazca Plate and facilitate the flat subduction beneath Chile.

4.2 "Peru-type" Flat Subduction

The flat subduction in Peru is commonly thought to have been caused by subduction of the Nazca Ridge (Antonijevic et al., 2015; Huangfu PP et al., 2016; Bishop et al., 2017). However, the thickness of the Nazca Ridge crust is 18 ± 3 km, and it has a maximum width of 200 km (Woods and Okal, 1994; Espurt et al., 2007), which could lead to a 185-km-long flat slab segment according to our model results (Figure 6). Thus, the Nazca Ridge would have had difficulty supporting the Peru flat slab segment, which is more than 300 km in length and 1,000 km in width (Gutscher et al., 1999; Manea et al., 2017). The Inca oceanic plateau, which has been totally subducted beneath the South American Plate, is located to the north of the Nazca Ridge (Gutscher et al., 1999; Espurt et al., 2008; Figure 1a). The parallel subduction of the Inca oceanic plateau and the Nazca Ridge could together provide enough buoyant force to support the Peru flat subduction zone, as shown in our model with double aseismic ridge subduction (Figure 8). Additionally, seismic observations revealed a sag of the subducting slab in the Peru subduction zone (Gutscher et al., 1999), coincident with our model predictions (Figure 8b). Furthermore, if we take the Peru–Chile subduction as a whole, the Nazca Ridge and Juan Fernández Ridge are interacting with the trench. However, the distance between these two aseismic ridges is up to 1,500 km, and no flat subduction has been observed between these two ridges. Thus, if the distance between two aseismic ridges is large, the influence on the slab dip angle between the two aseismic ridges will be limited (Figure S2).

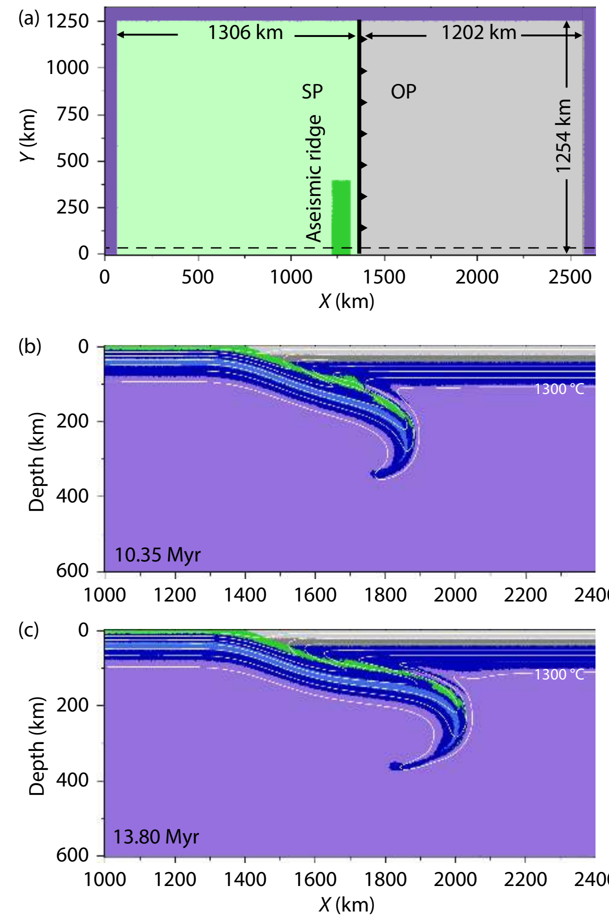

Figure 7. Model setup and results for the subduction of an aseismic ridge parallel to the trench. (a) Top view of the model with an aseismic ridge parallel to the trench. The aseismic ridge is 100 km long in the X direction, and its crust is 15 km thick. The impact width of the aseismic ridge is 800 km in the Y direction (half-width is 400 km in the model). SP, subducting plate; OP, overriding plate. The composition field and temperature contours along the dashed line in panel (a) at 10.35 Myr and 13.80 Myr are shown in panels (b) and (c), respectively.

In the Nankai subduction zone, the typical crustal thickness of the Izu–Bonin Arc is 20 km (Nishizawa et al., 2006), and the crustal

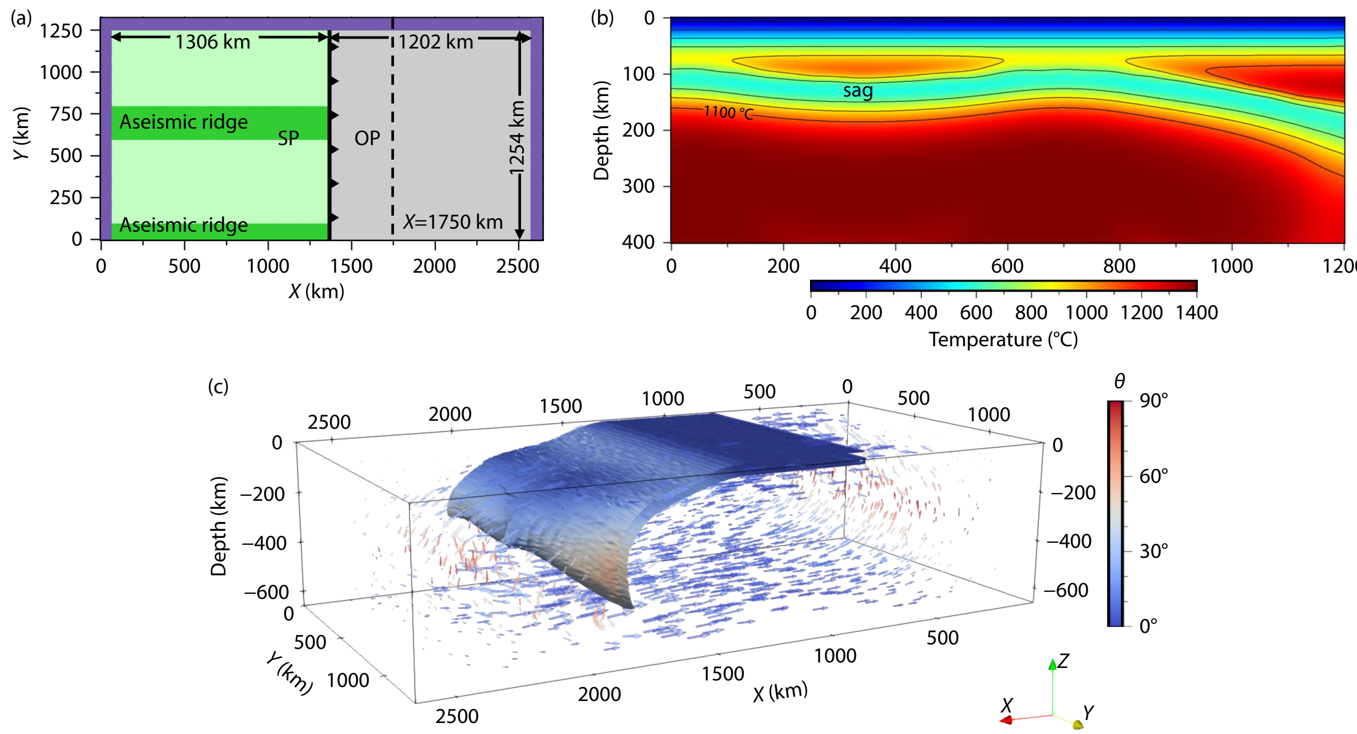

Figure 8. Model setup and results of the subduction of double aseismic ridges. (a) Top view of the model. The aseismic ridges are 200 km wide (half-width is 100 km at the boundary because of the reflective boundary condition), and their crust is 20 km thick. SP, subducting plate; OP, overriding plate. (b) The temperature field along the dashed line in panel (a), showing the morphology of the subducting slab at 13.80 Myr. (c) The morphology of the subducting slab and the distribution of the dynamic slab dip angle at 13.80 Myr, showing a large flat slab segment.

thickness varies along the narrow (<50 km) Palau–Kyushu Ridge from 15 to 22 km (Nishizawa et al., 2007). However, Gutscher (2001) suggested that the flat subduction of the Philippine Sea Plate beneath SW Japan is ~400 km long and ~600 km wide (Figure 1b). According to our model results, it is difficult for the Izu–Bonin Arc or the Palau–Kyushu Ridge alone to support such a large flat slab segment (Figure 6). However, similar to the Peru flat subduction, the Izu–Bonin Arc and the Palau–Kyushu Ridge form a parallel ridge subduction, which can provide enough buoyant force to support a flat slab segment during the subduction process of the Philippine Sea Plate (Gutscher, 2001; Figure 8).

The Laramide orogeny is thought to be strongly influenced by the flat subduction dynamics of the Farallon Plate (Liu LJ et al., 2010; Liu SB and Currie, 2016). By using a plate reconstruction model (Müller et al., 2008) and carrying out an inverse mantle convection model starting with a shear-wave seismic tomography model (Grand, 2002), Liu LJ et al. (2010) suggested that the Shatsky and Hess oceanic plateaus on the Farallon Plate intersected the North American Plate at ~90 Myr and ~70 Myr ago and that their accumulated crustal pile thickness could reach 50 km. Liu LJ et al. (2010) also suggested that the flat subduction of the Farallon Plate beneath the North American Plate during the Late Cretaceous could be explained by the buoyancy provided by the Shatsky and Hess oceanic plateaus and the increased plate coupling with the mantle wedge.

4.3 Tonga–Kermadec Subduction with No Flat Subduction

In the Tonga–Kermadec subduction zone, the Louisville Seamount Chain has been subducting beneath the Australian Plate for at least 4 Myr (Timm et al., 2013; Figure 1c), but no flat subduction has been detected (Bonnardot et al., 2007). The crustal thickness of the Louisville Seamount Chain is ~12 km, and its width is ~50 km (Contreras-Reyes et al., 2010). Thus, it is insufficient to induce flat subduction according to our model results (Figure 6). In addition, the collision of the Hikurangi Plateau at the southernmost part of the Tonga–Kermadec subduction zone would bring more complexity to the slab dip angle, which is necessary to explore with more complex models (Davy et al., 2008; He XB et al., 2022).

We can also observe that the Pacific Plate carries some other large-scale buoyant impactors to subduct beneath the Philippine Sea Plate, such as the Ogasawara Plateau, the Magellan Seamounts, and the Caroline Ridge (Lallemand et al., 2005; Tsuji et al., 2007; Mason et al., 2010). However, no flat subduction zone has been observed near these buoyant impactors, which may be due to the age of the subducting Pacific Plate. When the age of the subducting plate increases, it becomes denser, making it more difficult to form flat subduction, even though the buoyant impactor is relatively wide and thick (Figure S3). Furthermore, the eclogitization process may be a possible factor causing the absence of flat subduction near these buoyant impactors (Yan ZY et al., 2022).

5. Conclusions

In summary, we systematically investigated the influence of the aseismic ridge, especially its width and crustal thickness, on the formation of flat subduction. Our results suggest that the aseismic ridge must be wide and thick enough to cause notable flat subduction, a condition that is difficult to satisfy on Earth. We then suggest two alternative ways to meet this condition: (1) aseismic ridge subduction parallel to the trench and (2) double aseismic ridges acting together to support the flat slab segment. These two mechanisms can explain the formation of flat subduction beneath Chile, Peru, and other places.

Acknowledgments

This work is supported by the Strategic Priority Research Program of the Chinese Academy of Sciences (Grant No. XDB 41000000), the National Natural Science Foundation of China (Grant No. 41820104004), and the Fundamental Research Funds for the Central Universities (Grant No. WK2080000144). The topography data used to plot Figure 1 are from Tozer et al. (2019). The slab morphology contours in Figure 1 are from SLAB 2.0 (Hayes et al., 2018). The volcanism eruption data in Figure 1 are from the Global Volcanism Program (https://doi.org/10.5479/si.GVP.VOTW4-2013). The numerical code in this paper is modified from CitcomCU (Zhong SJ, 2006; Leng W and Gurnis, 2015), and codes are available through https://zenodo.org/record/7307308#.Y2t1GnZByNc.

Supplementary Materials

See FigureS1 to Figure S3.

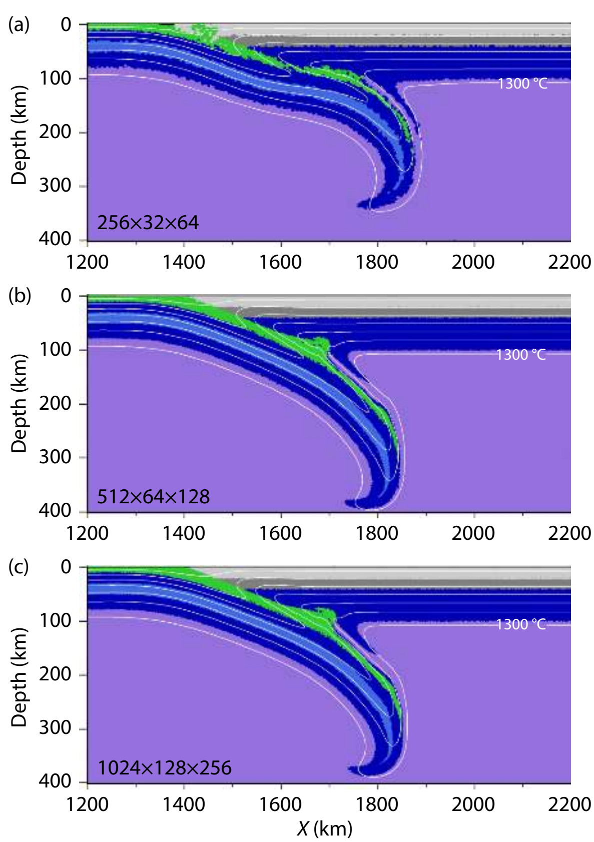

Figure S1. The results of models with different resolutions. The resolutions of these models are (a) 10.31 × 41.25 × 10.31 km (256 × 32 × 64 grids), (b) 5.16 × 20.63 × 5.16 km (512 × 64 × 128 grids), and (c) 2.58 × 10.31 × 2.58 km (1,024 × 128 × 256 grids), in the *X*, *Y*, and *Z* directions, respectively.

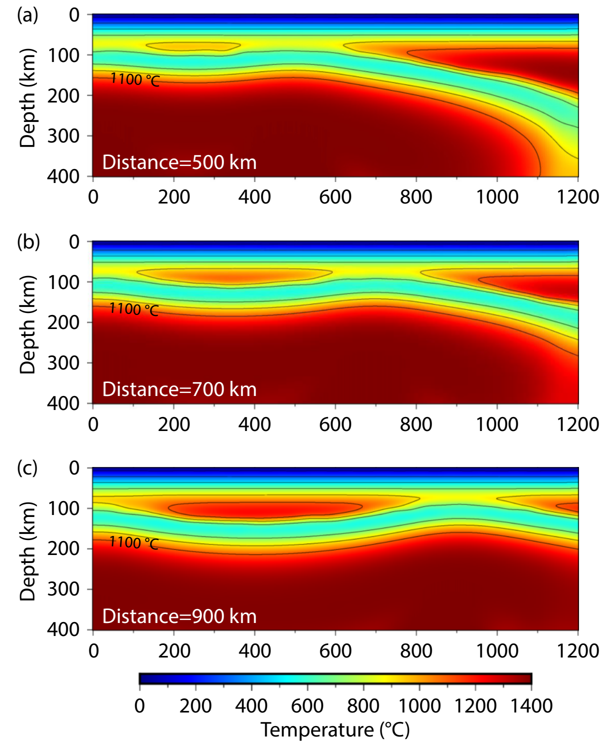

Figure S2. Temperature field along the dashed line in Figure 8a, showing the influence of the distance between two aseismic ridges on the subducting slab geometry. The distances between two aseismic ridges are (a) 500 km, (b) 700 km, and (c) 900 km, respectively.

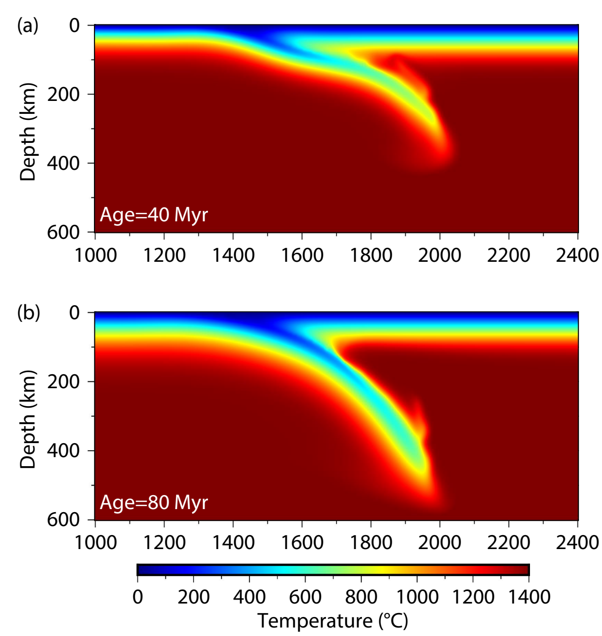

Figure S3. Temperature field along Profile 2 in Figure 2a, showing the influence of the subducting plate age on slab geometry. The aseismic ridge is 200 km wide, and its crustal thickness is 20 km, which is identical to the reference model (Figure 3). The age of the subducting plate is (a) 40 Myr and (b) 80 Myr. The slab dip angle increases when the age of the subducting plate increases.

References

Antonijevic, S. K., Wagner, L. S., Kumar, A., Beck, S. L., Long, M. D., Zandt, G., Tavera, H., and Condori, C. (2015). The role of ridges in the formation and longevity of flat slabs. *Nature*, *524*(7564), 212–215. https://doi.org/10.1038/nature14648

Bello-González, J. P., Contreras-Reyes, E., and Arriagada, C. (2018). Predicted path for hotspot tracks off South America since Paleocene times: Tectonic implications of ridge-trench collision along the Andean margin. *Gondwana Res.*, *64*, 216–234. https://doi.org/10.1016/j.gr.2018.07.008

Betts, P. G., Moresi, L., Miller, M. S., and Willis, D. (2015). Geodynamics of oceanic plateau and plume head accretion and their role in Phanerozoic orogenic systems of China. *Geosci. Front.*, *6*(1), 49–59. https://doi.org/10.1016/j.gsf.2014.07.002

Bishop, B. T., Beck, S. L., Zandt, G., Wagner, L., Long, M., Antonijevic, S. K., Kumar, A., and Tavera, H. (2017). Causes and consequences of flat-slab subduction in southern Peru. *Geosphere*, *13*(5), 1392–1407. https://doi.org/10.1130/Ges01440.1

Bodmer, M., Toomey, D. R., Hooft, E. E. E., and Schmandt, B. (2018). Buoyant asthenosphere beneath Cascadia influences megathrust segmentation. *Geophys. Res. Lett.*, *45*(14), 6954–6962. https://doi.org/10.1029/2018GL078700

Bonnardot, M. A., Régnier, M., Ruellan, E., Christova, C., and Tric, E. (2007). Seismicity and state of stress within the overriding plate of the Tonga-Kermadec subduction zone. *Tectonics*, *26*(5), TC5017. https://doi.org/10.1029/2006tc002044

Buck, W. R., and Poliakov, A. N. B. (1998). Abyssal hills formed by stretching oceanic lithosphere. *Nature*, *392*(6673), 272–275. https://doi.org/10.1038/32636

Capitanio, F. A., Faccenna, C., Zlotnik, S., and Stegman, D. R. (2011). Subduction dynamics and the origin of Andean orogeny and the Bolivian orocline. *Nature*, *480*(7375), 83–86. https://doi.org/10.1038/nature10596

Chen, Y. W., Wu, J., and Suppe, J. (2019). Southward propagation of Nazca subduction along the Andes. *Nature*, *565*(7740), 441–447. https://doi.org/10.1038/s41586-018-0860-1

Contreras-Reyes, E., Grevemeyer, I., Watts, A. B., Planert, L., Flueh, E. R., and Peirce, C. (2010). Crustal intrusion beneath the Louisville hotspot track. *Earth Planet. Sci. Lett.*, *289*(3–4), 323–333. https://doi.org/10.1016/j.epsl.2009.11.020

Davy, B., Hoernle, K., and Werner, R. (2008). Hikurangi Plateau: Crustal structure, rifted formation, and Gondwana subduction history. *Geochem. Geophys. Geosyst.*, *9*(7), Q07004. https://doi.org/10.1029/2007gc001855

Espurt, N., Baby, P., Brusset, S., Roddaz, M., Hermoza, W., Regard, V., Antoine, P. O., Salas-Gismondi, R., and Bolaños, R. (2007). How does the Nazca Ridge subduction influence the modern Amazonian foreland basin?. *Geology*, *35*(6), 515–518. https://doi.org/10.1130/g23237a.1

Espurt, N., Funiciello, F., Martinod, J., Guillaume, B., Regard, V., Faccenna, C., and Brusset, S. (2008). Flat subduction dynamics and deformation of the South American plate: Insights from analog modeling. *Tectonics*, *27*(3), TC3011. https://doi.org/10.1029/2007tc002175

Fan, J. K., and Zhao, D. P. (2021). Subslab heterogeneity and giant megathrust earthquakes. *Nat. Geosci.*, *14*(5), 349–353. https://doi.org/10.1038/s41561-021-00728-x

Flórez-Rodríguez, A. G., Schellart, W. P., and Strak, V. (2019). Impact of aseismic ridges on subduction systems: Insights from analog modeling. *J. Geophys. Res.: Solid Earth*, *124*(6), 5951–5969. https://doi.org/10.1029/2019jb017488

Gerya, T. V., Fossati, D., Cantieni, C., and Seward, D. (2009). Dynamic effects of aseismic ridge subduction: Numerical modelling. *Eur. J. Mineral.*, *21*(3), 649–661. https://doi.org/10.1127/0935-1221/2009/0021-1931

Glerum, A., Thieulot, C., Fraters, M., Blom, C., and Spakman, W. (2018). Nonlinear viscoplasticity in ASPECT: Benchmarking and applications to subduction. *Solid Earth*, *9*(2), 267–294. https://doi.org/10.5194/se-9-267-2018

Grand, S. P. (2002). Mantle shear-wave tomography and the fate of subducted slabs. *Phil. Trans. Roy. Soc. Lond. Ser. A: Math. Phys. Eng. Sci.*, *360*(1800), 2475–2491. https://doi.org/10.1098/rsta.2002.1077

Gutscher, M. A., Olivet, J. L., Aslanian, D., Eissen, J. P., and Maury, R. (1999). The "lost Inca Plateau": Cause of flat subduction beneath Peru?. *Earth Planet. Sci. Lett.*, *171*(3), 335–341. https://doi.org/10.1016/s0012-821x(99)00153-3

Gutscher, M. A., Spakman, W., Bijwaard, H., and Engdahl, E. R. (2000). Geodynamics of flat subduction: Seismicity and tomographic constraints from the Andean margin. *Tectonics*, *19*(5), 814–833. https://doi.org/10.1029/1999tc001152

Gutscher, M. A. (2001). An Andean model of interplate coupling and strain partitioning applied to the flat subduction zone of SW Japan (Nankai Trough). *Tectonophysics*, *333*(1–2), 95–109. https://doi.org/10.1016/S0040-1951(00)00269-9

Hampel, A., Adam, J., and Kukowski, N. (2004). Response of the tectonically erosive south Peruvian forearc to subduction of the Nazca Ridge: Analysis of three-dimensional analogue experiments. *Tectonics*, *23*(5), TC5003. https://doi.org/10.1029/2003tc001585

Hawley, W. B., Allen, R. M., and Richards, M. A. (2016). Tomography reveals buoyant asthenosphere accumulating beneath the Juan de Fuca plate. *Science*, *353*(6306), 1406–1408. https://doi.org/10.1126/science.aad8104

Hayes, G. P., Moore, G. L., Portner, D. E., Hearne, M., Flamme, H., Furtney, M., and Smoczyk, G. M. (2018). Slab2, a comprehensive subduction zone geometry model. *Science*, *362*(6410), 58–61. https://doi.org/10.1126/science.aat4723

He, X. B., Tao, J. T., Cao, Y., Pan, F. B., He, E. Y., Cao, L. M., and Zheng, Y. X. (2022). No seamount subduction, no magmatic arc?. *Earth Planet. Phys.*, *6*(4), 424–429. https://doi.org/10.26464/epp2022031

Horton, B. K. (2018). Tectonic regimes of the Central and Southern Andes: Responses to variations in plate coupling during subduction. *Tectonics*, *37*(2), 402–429. https://doi.org/10.1002/2017tc004624

Hu, J. S., Liu, L. J., and Zhou, Q. (2018). Reproducing past subduction and mantle flow using high-resolution global convection models. *Earth Planet. Phys.*, *2*(3), 189–207. https://doi.org/10.26464/epp2018019

Hu, J. S., Liu, L. J., Hermosillo, A., and Zhou, Q. (2016). Simulation of late Cenozoic South American flat-slab subduction using geodynamic models with data assimilation. *Earth Planet. Sci. Lett.*, *438*, 1–13. https://doi.org/10.1016/j.epsl.2016.01.011

Huangfu, P. P., Wang, Y. J., Cawood, P. A., Li, Z. H., Fan, W. M., and Gerya, T. V. (2016). Thermo-mechanical controls of flat subduction: Insights from numerical modeling. *Gondwana Res.*, *40*, 170–183. https://doi.org/10.1016/j.gr.2016.08.012

Jang, H., Kim, Y., Lim, H., and Clayton, R. W. (2019). Seismic attenuation structure of southern Peruvian subduction system. *Tectonophysics*, *771*, 228203. https://doi.org/10.1016/j.tecto.2019.228203

Jischke, M. C. (1975). On the dynamics of descending lithospheric plates and slip zones. *J. Geophys. Res.*, *80*(35), 4809–4813. https://doi.org/10.1029/JB080i035p04809

Kay, S. M., and Mpodozis, C. (2002). Magmatism as a probe to the Neogene shallowing of the Nazca plate beneath the modern Chilean flat-slab. *J. South Amer. Earth Sci.*, *15*(1), 39–57. https://doi.org/10.1016/S0895-9811(02)00005-6

Kopp, H., Flueh, E. R., Papenberg, C., and Klaeschen, D. (2004). Seismic investigations of the O'Higgins Seamount Group and Juan Fernández Ridge: Aseismic ridge emplacement and lithosphere hydration. *Tectonics*, *23*(2), TC2009. https://doi.org/10.1029/2003tc001590

Lallemand, S., Heuret, A., and Boutelier, D. (2005). On the relationships between slab dip, back-arc stress, upper plate absolute motion, and crustal nature in subduction zones. *Geochem. Geophys. Geosyst.*, *6*(9), Q09006. https://doi.org/10.1029/2005gc000917

Leng, W., and Gurnis, M. (2011). Dynamics of subduction initiation with different evolutionary pathways. *Geochem. Geophys. Geosyst.*, *12*(12), Q12018. https://doi.org/10.1029/2011gc003877

Leng, W., and Gurnis, M. (2015). Subduction initiation at relic arcs. *Geophys. Res. Lett.*, *42*(17), 7014–7021. https://doi.org/10.1002/2015gl064985

Li, Z. X., and Li, X. H. (2007). Formation of the 1300-km-wide intracontinental orogen and postorogenic magmatic province in Mesozoic South China: A flat-slab subduction model. *Geology*, *35*(2), 179–182. https://doi.org/10.1130/g23193a.1

Linkimer, L., Beck, S., Zandt, G., Alvarado, P., Anderson, M., Gilbert, H., and

Zhang, H. J. (2020). Lithospheric structure of the Pampean flat slab region from double-difference tomography. *J. South Amer. Earth Sci.*, *97*, 102417. https://doi.org/10.1016/j.jsames.2019.102417

Liu, L. J., Gurnis, M., Seton, M., Saleeby, J., Müller, R. D., and Jackson, J. M. (2010). The role of oceanic plateau subduction in the Laramide orogeny. *Nat. Geosci.*, *3*(5), 353–357. https://doi.org/10.1038/ngeo829

Liu, S. B., and Currie, C. A. (2016). Farallon plate dynamics prior to the Laramide orogeny: Numerical models of flat subduction. *Tectonophysics*, *666*, 33–47. https://doi.org/10.1016/j.tecto.2015.10.010

Manea, V. C., Manea, M., Ferrari, L., Orozco-Esquivel, T., Valenzuela, R. W., Husker, A., and Kostoglodov, V. (2017). A review of the geodynamic evolution of flat slab subduction in Mexico, Peru, and Chile. *Tectonophysics*, *695*, 27–52. https://doi.org/10.1016/j.tecto.2016.11.037

Martinod, J., Guillaume, B., Espurt, N., Faccenna, C., Funiciello, F., and Regard, V. (2013). Effect of aseismic ridge subduction on slab geometry and overriding plate deformation: Insights from analogue modeling. *Tectonophysics*, *588*, 39–55. https://doi.org/10.1016/j.tecto.2012.12.010

Mason, W. G., Moresi, L., Betts, P. G., and Miller, M. S. (2010). Three-dimensional numerical models of the influence of a buoyant oceanic plateau on subduction zones. *Tectonophysics*, *483*(1–2), 71–79. https://doi.org/10.1016/j.tecto.2009.08.021

Moresi, L., Betts, P. G., Miller, M. S., and Cayley, R. A. (2014). Dynamics of continental accretion. *Nature*, *508*(7495), 245–248. https://doi.org/10.1038/nature13033

Müller, R. D., Sdrolias, M., Gaina, C., and Roest, W. R. (2008). Age, spreading rates, and spreading asymmetry of the world's ocean crust. *Geochem. Geophys. Geosyst.*, *9*(4), Q04006. https://doi.org/10.1029/2007gc001743

Müller, R. D., Seton, M., Zahirovic, S., Williams, S. E., Matthews, K. J., Wright, N. M., Shephard, G. E., Maloney, K. T., Barnett-Moore, N., … Cannon, J. (2016). Ocean basin evolution and global-scale plate reorganization events since pangea breakup. *Annu. Rev. Earth Planet. Sci.*, *44*, 107–138. https://doi.org/10.1146/annurev-earth-060115-012211

Nishizawa, A., Kaneda, K., Nakanishi, A., Takahashi, N., and Kodaira, S. (2006). Crustal structure of the ocean-island arc transition at the mid Izu-Ogasawara (Bonin) arc margin. *Earth Planets Space*, *58*(8), E33–E36. https://doi.org/10.1186/bf03352594

Nishizawa, A., Kaneda, K., Katagiri, Y., and Kasahara, J. (2007). Variation in crustal structure along the Kyushu-Palau Ridge at 15–21°N on the Philippine Sea plate based on seismic refraction profiles. *Earth Planets Space*, *59*(6), E17–E20. https://doi.org/10.1186/bf03352711

Oryan, B., and Buck, W. R. (2020). Larger tsunamis from megathrust earthquakes where slab dip is reduced. *Nat. Geosci.*, *13*(4), 319–324. https://doi.org/10.1038/s41561-020-0553-x

Pesicek, J. D., Engdahl, E. R., Thurber, C. H., DeShon, H. R., and Lange, D. (2012). Mantle subducting slab structure in the region of the 2010 *M*8.8 Maule earthquake (30–40°S), Chile. *Geophys. J. Int.*, *191*(1), 317–324. https://doi.org/10.1111/j.1365-246X.2012.05624.x

Portner, D. E., Beck, S., Zandt, G., and Scire, A. (2017). The nature of subslab slow velocity anomalies beneath South America. *Geophys. Res. Lett.*, *44*(10), 4747–4755. https://doi.org/10.1002/2017gl073106

Ramos, V. A., Cristallini, E. O., and Pérez, D. J. (2002). The Pampean flat-slab of the Central Andes. *J. South Amer. Earth Sci.*, *15*(1), 59–78. https://doi.org/10.1016/S0895-9811(02)00006-8

Ranalli, G. (1995). *Rheology of the Earth* (2nd ed). Dordrecht: Springer.

Rodríguez-González, J., Billen, M. I., and Negredo, A. M. (2014). Non-steady-state subduction and trench-parallel flow induced by overriding plate structure. *Earth Planet. Sci. Lett.*, *401*, 227–235. https://doi.org/10.1016/j.epsl.2014.06.013

Schellart, W. P., and Moresi, L. (2013). A new driving mechanism for backarc extension and backarc shortening through slab sinking induced toroidal and poloidal mantle flow: Results from dynamic subduction models with an overriding plate. *J. Geophys. Res.: Solid Earth*, *118*(6), 3221–3248. https://doi.org/10.1002/jgrb.50173

Skinner, S. M., and Clayton, R. W. (2011). An evaluation of proposed mechanisms of slab flattening in Central Mexico. *Pure Appl. Geophys.*, *168*(8–9), 1461–1474. https://doi.org/10.1007/s00024-010-0200-3

Taramón, J. M., Rodríguez-González, J., Negredo, A. M., and Billen, M. I. (2015). Influence of cratonic lithosphere on the formation and evolution of flat slabs: Insights from 3-D time-dependent modeling. *Geochem. Geophys. Geosyst.*, *16*(9), 2933–2948. https://doi.org/10.1002/2015gc005940

Tetreault, J. L., and Buiter, S. J. H. (2012). Geodynamic models of terrane accretion: Testing the fate of island arcs, oceanic plateaus, and continental fragments in subduction zones. *J. Geophys. Res.: Solid Earth*, *117*(B8), B08403. https://doi.org/10.1029/2012jb009316

Timm, C., Bassett, D., Graham, I. J., Leybourne, M. I., de Ronde, C. E. J., Woodhead, J., Layton-Matthews, D., and Watts, A. B. (2013). Louisville seamount subduction and its implication on mantle flow beneath the central Tonga-Kermadec arc. *Nat. Commun.*, *4*, 1720. https://doi.org/10.1038/ncomms2702

Tozer, B., Sandwell, D. T., Smith, W. H. F., Olson, C., Beale, J. R., and Wessel, P. (2019). Global bathymetry and topography at 15 arc sec: SRTM15+. *Earth Space Science*, *6*(10), 1847–1864. https://doi.org/10.1029/2019ea000658

Tsuji, T., Nakamura, Y., Tokuyama, H., Coffin, M. F., and Koda, K. (2007). Oceanic crust and Moho of the Pacific plate in the eastern Ogasawara Plateau region. *Island Arc*, *16*(3), 361–373. https://doi.org/10.1111/j.1440-1738.2007.00589.x

van Hunen, J., van den Berg, A. P., and Vlaar, N. J. (2002). The impact of the South-American plate motion and the Nazca Ridge subduction on the flat subduction below South Peru. *Geophys. Res. Lett.*, *29*(14), 35-1–35-4. https://doi.org/10.1029/2001gl014004

Vogt, K., and Gerya, T. V. (2014). From oceanic plateaus to allochthonous terranes: Numerical modelling. *Gondwana Res.*, *25*(2), 494–508. https://doi.org/10.1016/j.gr.2012.11.002

Woods, M. T., and Okal, E. A. (1994). The structure of the Nazca ridge and Sala Y Gomez seamount chain from the dispersion of Rayleigh waves. *Geophys. J. Int.*, *117*(1), 205–222. https://doi.org/10.1111/j.1365-246X.1994.tb03313.x

Yan, Z. Y., Chen, L., Xiong, X., Wang, K., Xie, R. X., and Hsu, H. T. (2020). Observations and modeling of flat subduction and its geological effects. *Sci. China Earth Sci.*, *63*(8), 1069–1091. https://doi.org/10.1007/s11430-019-9575-2

Yan, Z. Y., Chen, L., Xiong, X., Wan, B., and Xu, H. Z. (2021). Oceanic plateau and subduction zone jump: Two-dimensional thermo-mechanical modeling. *J. Geophys. Res.: Solid Earth*, *126*(7), e2021JB021855. https://doi.org/10.1029/2021jb021855

Yan, Z. Y., Chen, L., Zuza, A. V., Tang, J. X., Wan, B., and Meng, Q. R. (2022). The fate of oceanic plateaus: Subduction versus accretion. *Geophys. J. Int.*, *231*(2), 1349–1362. https://doi.org/10.1093/gji/ggac266

Yáñez, G. A., Ranero, C. R., von Huene, R., and Díaz, J. (2001). Magnetic anomaly interpretation across the southern central Andes (32°–34°S): The role of the Juan Fernández Ridge in the late Tertiary evolution of the margin. *J. Geophys. Res.: Solid Earth*, *106*(B4), 6325–6345. https://doi.org/10.1029/2000jb900337

Zhao, H., Shen, X. B., and Leng, W. (2021). Evolution of subduction cusps from the perspective of trench migration and slab morphology. *Front. Earth Sci.*, *9*, 783409. https://doi.org/10.3389/feart.2021.783409

Zhong, S. J. (2006). Constraints on thermochemical convection of the mantle from plume heat flux, plume excess temperature, and upper mantle temperature. *J. Geophys. Res.: Solid Earth*, *111*(B4), B04409. https://doi.org/10.1029/2005jb003972